High-speed imaging of degassing kinetics of CO2–water mixtures

Boeije, C.S.; Zitha, P.L.J.; Pluymakers, A.M.H.

Important note
To cite this publication, please use the final published version (if applicable).
Please check the document version above.

High-speed imaging of degassing kinetics of CO_2–water mixtures

Chris Boeije, Pacelli Zitha and Anne Pluymakers

View Online   Export Citation   CrossMark

ARTICLES YOU MAY BE INTERESTED IN

Physics of Fluids

Special Topic: Food Physics

Submit Today!

AIP Publishing

High-speed imaging of degassing kinetics of CO$_2$–water mixtures

View Online   Export Citation   CrossMark

Chris Boeije,[a] (ID) Pacelli Zitha, (ID) and Anne Pluymakers (ID)

AFFILIATIONS

Department of Geoscience & Engineering, Delft University of Technology, Stevinweg 1, 2628 CN Delft, The Netherlands

[a] Author to whom correspondence should be addressed: c.s.boeije@tudelft.nl

ABSTRACT

The exsolution of gas molecules from gas–liquid mixtures plays a significant role in a wide range of applications from industrial processes such as metal casting to subsurface flow of oil or geothermal waters. This study aims to improve the understanding of the conditions under which free gas bubbles start forming in CO$_2$–water mixtures. The bubble point pressure was determined under various different conditions like the temperature and initial pressure of the mixture along with other parameters such as the bubble growth rate. A series of depressurization experiments at high pressure and temperature (up to 100 bar and 100 °C) is performed using a pressure cell that allows for visual monitoring of the degassing process. Bubble formation during the depressurization process is recorded using a high-speed camera paired with a uniform light source along with a pressure transducer and thermocouple. Image analysis allows for the determination of the bubble point pressure and rate of bubble formation. For CO$_2$ in its gaseous state and at moderate temperatures, decent agreement between experimental results and the theoretical bubble point pressure is found, although significant deviations are observed at elevated temperatures. More pronounced differences in bubble point are observed for mixtures starting out at high pressures where CO$_2$ is a supercritical fluid, which lead to lower than expected bubble point pressures.

I. INTRODUCTION

Degassing is a process where free gas bubbles nucleate from a fluid-containing dissolved gases. Bubbles form due to a change in the equilibrium conditions in the mixture that affect the gas solubility, such as a change in pressure or temperature.[1,2] In addition, degassing can also occur by exsolution of gas through a liquid–gas interface (without bubbling), as is the case in carbonated beverages.[3]

A. Applications of degassing

Degassing of fluids plays a role in a variety of industrial and natural processes on a large range of scales, ranging in scale all the way from microfluidic devices to subsurface flows in reservoirs and volcanoes. In microfluidic systems, degassing can lead to trapping of air bubbles whenever fluids are pumped, which can block flow paths or sensor surfaces.[4,5] Since here bubbles have the same dimensions as the flow channels, the liquid flow is limited or blocked entirely, because of surface tension.[6] This can also cause increased flow-induced shear stress,[7] which can be damaging when used in setups involving delicate materials such as living cells. During metal casting, for example, for aluminum production, hydrogen bubbles may become trapped in the melt causing metal to become porous, which is detrimental for its mechanical properties.[8,9] A common practice to prevent this is to degas the molten metal using ultrasonic actuation. This increases diffusion of gas through the melt to the free gas bubbles, thereby increasing their size and allowing them to rise through the liquid and dissipate.[10,11] Degassing is essential for foam injection molding. In this process, a gas–polymer mixture is injected into a mold at high pressure and then fills the cavity by reducing the pressure and allowing the gas to expand and fill the void. Pressure and injection speed govern the bubble nucleation and growth mechanisms and thus the structure of the foamed parts.[12–14] Degassing has several implications in oil production. For one, free CO$_2$ bubbles can cause more favorable conditions for the precipitation of calcium carbonate scale. In a hydrogeochemical model up to 12 times, more scaling was found for scenarios that incorporate degassed CO$_2$ compared to scenarios that do not.[15] Under oil well conditions, CO$_2$ degassing is estimated to be responsible for 60% to 90% of carbonate scaling,[16] leading to production problems.[17] The exsolution of gas can also improve oil recovery as the gas reduces the hydrostatic pressure in the well, thereby lifting

the other fluids to the surface (gas lift).[18,19] Furthermore, gas exsolution from carbonated water is found to lead to oil mobilization, which can also increase recovery.[20] Degassing also occurs during the production of geothermal brines. These are typically saturated with calcium ions, and thus, calcite precipitation also occurs in geothermal wells, similarly to oil wells.[21–23] Corrosion is also expected to occur in both geothermal and oil wells, for chemically active gases such as CO_2 or H_2.[24] Another issue for geothermal water production is that the formation of free gas can cause reduction of the water relative permeability in reservoirs, thus limiting the production rate of these waters. The Groß Schönebeck field in Germany saw a 93% decrease in its productivity index from June 2011 to November 2013 for which the presence of free gas in the near-well region was considered a likely cause.[25] Surveys of CO_2 degassing in soils have also been used to explore the potential of various sites in Italy[26,27] and the Canary Islands[28] to contain geothermal resources, and in the Los Humeros field in Mexico, regions of high degassing were found to indicate the presence of high-permeability faults.[29] On large time scales, degassing is also known to cause significant CO_2 emissions into the atmosphere,[23,30,31] but can also enhance microbial life in the subsurface.[32] Similar methods were also employed to analyze the rates of degassing from the Mount Etna volcano[33] and assess its magmatic reservoir pressure.[34]

B. Objectives of study

This study aims to provide high-quality data and analysis on the emergence of free CO_2 bubbles from fluids along with the development of the bubble population during a depressurization process, under temperature, pressure, and concentrations relevant to low-temperature geothermal water production. Most of the literature relevant to degassing of geothermal brines is related to the solubility of gases in these brines. Various sets of solubility measurement data are available in the literature for CO_2 solubility in NaCl and $CaCl_2$ solutions[35–37] or focus on the modeling of such systems.[38–40] However, the bubble nucleation process and bubble population development at conditions relevant to geothermal water production have not been studied extensively thus far.

The main research topics that are addressed here are the dependency of the bubble point pressure on the various initial conditions and the parameters that control the evolution of the bubble population. To this end, a series of experiments is performed where a high-pressure CO_2–water mixture is depressurized inside a visual cell. A high-speed camera is used to visually monitor the process of bubble nucleation and simultaneously pressure and temperature are logged.

C. Background theory

Within this study, degassing is considered in the form of gas exsolution leading to bubble nucleation as this is the most relevant to the production of geothermal waters. Two bubble nucleation mechanisms are commonly distinguished: homogeneous vs heterogeneous nucleation.[41] Heterogeneous nucleation occurs on impurities on surfaces or specks of dust which function as nucleation sites for bubbles to form. Homogeneous nucleation happens in pure liquids, where such nucleation sites are not present making it more difficult for bubbles to form and liquids can be reduced in pressure considerably below the saturation vapor pressure without any bubble formation.[42] Heterogeneous nucleation is considered the dominant bubble formation mechanism in this

study due to the presence of surface imperfections within the experimental apparatus.

The solubility of CO_2 in water is proportional to the partial pressure of CO_2 and follows Henry's law. Thus, for the production of geothermal waters, where the pressure reduces as it flows toward the production well, the solubility threshold can be exceeded leading to a supersaturated state. If the gas cannot exsolve from the solution through an existing gas–liquid interface, bubbles may start to nucleate. To start the heterogeneous nucleation process, surface imperfections with a large radius of curvature are required to overcome the required energy barrier. This critical radius of curvature is a function of the interfacial tension between liquid and gas and the concentration of CO_2 in the liquid.[43] As the pressure is reduced further, the degree to which the solution is supersaturated (i.e., its supersaturation ratio) increases controls, which leads to an increase in the rate at which bubbles are formed.[44]

II. MATERIALS AND METHODS

Experiments performed in this study focus on the formation of free CO_2 bubbles during depressurization mimicking the changes in pressure experienced in a geothermal well. The experiments were done at temperatures ranging from 20 to 100 °C, where the elevated temperatures are representative of low-enthalpy geothermal sites. This section describes the experimental setup used in this study and outlines the steps taken both during the experiments and the subsequent data analysis approach.

A. Experimental setup

Figure 1 shows a schematic of the experimental setup that is used in these experiments. The setup consists of the following components: a Chandler Engineering Quizix QX6000 dual piston pump allows for pumping water at high pressure. A Proserv Prolight 002990 titanium transfer vessel with a magnetic stirrer is used for creating gas–liquid mixtures. A stainless steel, high-pressure visual cell with two borosilicate sight glasses on either side to allow for the visualization of the flow inside. These sight glasses are circular, and the aperture available for visualization is 30 mm in diameter. This 30 mm is also the diameter of the cell's cylindrical internal volume, and it has a depth of 11.6 mm. Fluid inlet and outlet are located at bottom and top of the cell, respectively (cf. Fig. 2). A LED light source is installed to allow for uniform illumination of the cell's inner volume. A heating spiral is wrapped around the cell such that it can be heated up to the desired temperature in combination with a PID thermo-controller.

A Photron FASTCAM Mini UX100 camera is installed in front of the cell's window for high-speed imaging of the contents of the cell. This camera is used here at a rate of 500 frames per second. The camera is paired with a Nikon AF-S Nikkor 18–105 mm. This lens is meant for use with consumer Nikon digital cameras that have a larger sensor than the one present in the Photron camera used here. This means its image circle is considerably larger than is required to fill the frame, which means that light falloff in the corners of the image is virtually non-existent. The lens is used at a focal length of approximately 55 mm and an aperture of 1:3.5. These settings allow for the camera to be placed some distance away from the cell window, which is necessary for use at elevated temperature.

A Druck PTX 611 pressure transducer is connected to the cell to monitor the pressure during the experiments at a frequency of 100 Hz.
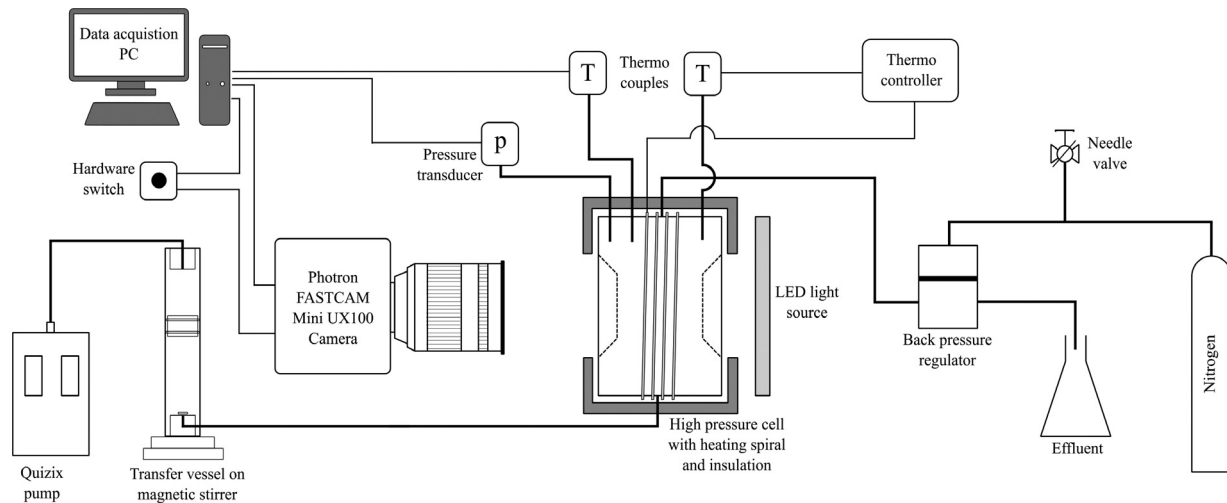
FIG. 1. Schematic of experimental setup.

Two thermo-couples are connected to the cell as well: one for connecting to the thermo-controller and one to a data acquisition PC. The system's pressure is controlled using a Mity Mite S-91W gas-loaded back pressure regulator combined with a nitrogen gas bottle. A needle valve within the back-pressure tubing allows for releasing the pressure in a controlled and reproducible manner. A hardware switch is connected to both the camera and the data acquisition PC, which is used to synchronize the captured images from the camera and the pressure and temperature logs.

B. Experimental procedure

Prior to starting the experiments, DI water and CO_2 are premixed in the desired proportions and pressure in the transfer vessel
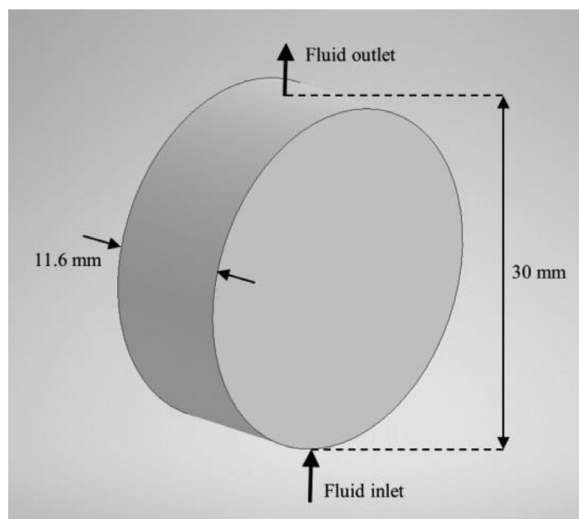

FIG. 2. Cylindrical internal volume of pressure cell with fluid inlet and outlet indicated along with relevant dimensions.

and then homogenized using a magnetic stirrer. The visual cell is initially pressurized by filling it with DI water. Subsequently, the water–CO_2 mixture can be pumped from the transfer vessel into the cell, displacing the initial DI water. To ensure that the cell contains only the CO_2–water mixture at the appropriate concentration, the total volume of water–CO_2 mixture that is pumped into the cell is five times the cell volume. During elevated temperature experiments, the cell is then heated to the desired temperature using the heating spiral.

Once the desired conditions are reached, the depressurization process can commence by opening a needle valve in the back-pressure system. This allows for a controlled and reproducible manner of reducing the system pressure. At a certain point during this process, the first free CO_2 bubbles emerge from the solution. The pressure at which this occurs is the bubble point pressure. The bubble formation process is captured in a series of images using the high-speed camera. Around 18 500 images are captured for each experiment at a resolution of 640 × 480 pixels. When the 30 mm sight glass fills the entire image, this means that the pixel size is approximately 62 μm (=30 mm/480 pixels), which is also the minimum bubble size that can be identified. The number of images and the rate of capture mean that the total duration of each experiment is around 37 s, which is enough for the full depressurization process to be performed. The image capturing sequence is ended by pressing a hardware switch, which simultaneously sends a pulse to the data acquisition PC to allow for the synchronization of images with the pressure and temperature data.

C. Data analysis methods

The main result from each experiment is a set of images that show the emergence and evolution of bubbles during the degassing process. An image analysis routine was developed using the MATLAB Image Processing Toolbox to identify individual bubbles and their properties such as size and growth rate. Since the images captured during the experiment and the pressure log are synchronized, the bubble data from the analyzed images are combined with the pressure data to determine at which pressure bubbles are formed during the degassing process.

The image analysis method is the following: first, the background image (i.e., the image at the start of the experiment before bubble formation) is subtracted resulting in net images with bubbles showing up as regions of high intensity. A global intensity threshold is used to convert these net images to a binary format. Individual bubbles are identified in these images using MATLAB's regionprops function, which uses pixel connectivity to determine whether pixels are part of the same region. Single-pixel regions could be caused by digital noise that can impact the results; thus, only regions of two or more pixels are considered in the remainder of the analysis.

A distinction is made between trapped bubbles that are growing on the cell's surfaces and free flowing bubbles inside the cell. This is done by comparing consecutive images with each other. If there is no difference in the position of a bubble compared to its position five frames earlier, that bubble is considered trapped. Finally, the number of bubbles (i.e., individual regions) is counted on every image and can be plotted as a function of pressure. The pressure at which the first bubble emerges from the solution is the bubble point pressure. Further analysis of the bubbles on the images allows for assessing the bubbles' growth rate by computing the equivalent diameter using $D_{eq} = \sqrt{4A/\pi}$, where A is the measured bubble area. Both the average growth rate of the bubbles due to gas expansion as a result of the depressurization and the growth of ascending individual bubbles due to gas diffusion to the bubble were investigated.

D. Overview of experiments

Several experiments were performed in this study with a range of different initial conditions. The conditions that were varied include initial pressure, temperature, and gas concentration. All experiments here were carried out using DI water as the aqueous phase. Experiments performed at ambient temperature only consist of the depressurization process, whereas elevated temperature experiments also contain the heating stage prior to depressurization.

Table I shows an overview of the experiments that were carried out within this study. All of these were performed by dissolving CO_2 in water at a certain pressure and monitoring the degassing that takes place due to depressurization. The initial mixing of water and CO_2 in the transfer vessel is performed at ambient temperature after which the fluid mixture is pumped into the cell and heated. This means that for high-pressure experiments using CO_2, the CO_2 is actually initially

liquid and undergoes a phase transition to a supercritical state during the heating stage ($p_{crit,CO2} = 73.8$ bar, $T_{crit,CO2} = 31.0\,°C$). The state of the CO_2 at the beginning of the depressurization process is stated explicitly in the table.

The main parameter studied here is the occurrence of the first free bubble as a function of the temperature and initial pressure of the mixture (see Subsection III A). Further details of the degassing process, such as the evolution of bubble size and influence of other experimental parameters, like the rate of depressurization are discussed in Subsection III B. A general discussion of the bubble formation process is presented in Subsection III C.

III. RESULTS AND DISCUSSION

A. Bubble point pressure

Most of the experiments discussed, here, were performed using solutions of CO_2 in brine at a concentration of 0.2 mol/l. This concentration was chosen for two main reasons. First, it is significantly lower than the fully saturated solution at ambient temperature. This ensures that no bubbles form during the heating stage for most of the experiments, which could obscure the interpretation of the depressurization process. Second, this concentration is representative for geothermal reservoirs, for which typically CO_2 concentrations range from 0.0114 to 0.227 mol/l.[45] For certain fields, CO_2 concentrations as high as 0.772 mol/l were found.[46] Experiments done at much higher CO_2 concentration (1.01 mol/l) are discussed in Sec. III B. These experiments were performed to assess the influence of the initial fluid in the visual cell on the degassing process.

Figure 3 (Multimedia view) compares the bubble point pressure, that is, the pressure at which the first bubbles are observed, for the experiments with initial CO_2 concentration of 0.2 mol/l. During these experiments, the temperature and the initial pressure were varied. The attached video shows an example of the image analysis method for the experiment starting at 100 bar and 100 °C.

In all experiments except the one at 30-bar experiment at 100 °C, the solubility limit for CO_2 in water was not exceeded during the heating stage so that no free gas bubbles were formed prior to the depressurization process. For the 30 bar/100 °C experiment, bubbles were formed during the heating sequence, implying that for this

TABLE I. Overview of experimental conditions for elevated temperature experiments.

Initial pressure (bar)	Temperature (°C)	Initial CO_2 concentration (mol/l)	Phase state of dissolved CO_2
30	20, 40, 60, 100	0.200	Gas
50	20, 40, 60, 100	0.200	Gas
100	20, 40, 60, 100	0.200	Liquid or supercritical
30	20	1.01[a]	Gas[b]

[a]This is a fully saturated solution; that is, this is the maximum CO_2 that can be dissolved at this pressure.
[b]This is a series of experiments using different initial fluids to assess its influence on the degassing process.
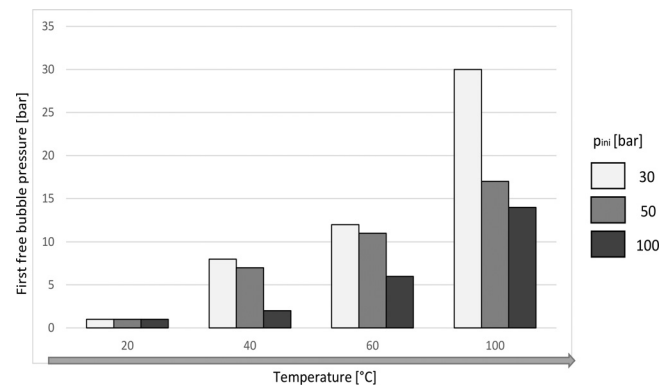

FIG. 3. First free bubble pressure for the CO_2 depressurization experiments vs temperature for an initial CO_2 concentration of 0.2 mol/l at three initial pressures, 30, 50, and 100 bar as indicated by the bars' grayscale. Multimedia view: https://doi.org/10.1063/5.0124500.1

experiment, the CO_2 concentration exceeded the CO_2 solubility limit. This means that in this case, free gas bubbles are present right from the start of the experiment. The solubility of CO_2 at elevated temperature can be estimated using Henry's law in combination with the van't Hoff equation.[47] The latter equation accounts for the temperature dependence of the gas solubility and is given in the following equation:

$$H(T) = H^0 \exp\left[\frac{-\Delta_{sol}H}{R}\left(\frac{1}{T} - \frac{1}{T^0}\right)\right], \tag{1}$$

where H^0 is Henry's constant at 25 °C, which for CO_2 is 3.4×10^{-2} mol/(l atm) and $-\Delta_{sol}H$ refers to enthalpy (i.e., the H is not equivalent to Henry's constant) with $\frac{-\Delta_{sol}H}{R}$ equal to 2400 K for CO_2. The solubility diagram, represented as contours of constant solubility for gaseous CO_2–water mixtures, obtained with Eq. (1) is shown in Fig. 4. The solubility of CO_2 in water was calculated for many values of pressure and temperature using the van't Hoff equation [Eq. (1)]. Subsequently, a contour fitting routine was employed to determine the iso-solubility contours that are given in the figure. The 0.2 mol/l contour is given in bold in this figure as this is the concentration used in most of these experiments, which is why theoretically this is where the first free gas bubble is expected. At pressures below this contour, the CO_2 solubility is less, so gas exsolution is expected. The phase diagram of CO_2 is superimposed on this figure to underscore the fact that the equation applies for gaseous CO_2. The experiments performed here are also shown in this figure as lines starting at the initial conditions (indicated by the symbol circles) and ending at the bubble point pressure (indicated by the symbol squares).

The figure shows that the solubility of CO_2 at 30 bar and 100 °C is nearly equal to 0.2 mol/l, explaining why a few free gas bubbles were already formed during the heating stage. The equation thus explains why no free gas bubbles were formed during the heating stage for the other experiments that are performed either at higher initial pressure or lower temperature, both of which lead to an increased CO_2 solubility.

The depressurization path for the 30 bar/40 °C experiment shows the first bubble forming around 8 bar, which coincides with the 0.2 mol/l contour, implying that for these conditions, the van't Hoff
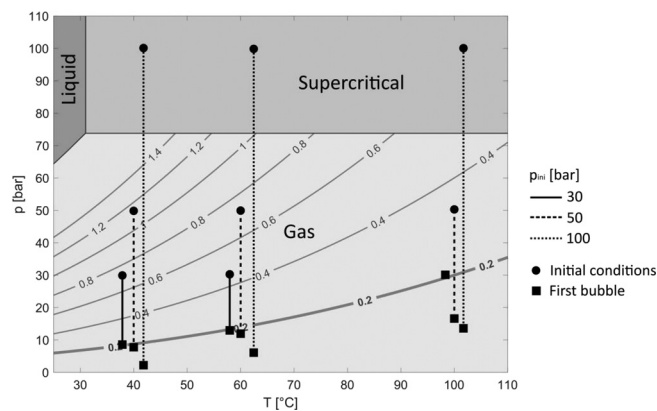
FIG. 4. Iso-solubility contours for CO_2 dissolved in brine (mol/l) as a function of temperature and pressure superposed on the CO_2 phase diagram. The 0.2 mol/l contour is shown as a thicker line, because this is the concentration that was used in these experiments. The vertical lines in the figure indicate the depressurization path for the experiments conducted in this study.

equation accurately predicts the bubble point pressure. This is not the case for the experiment that start out under supercritical conditions ($p_{ini} = 100$ bar). Despite using the same 0.2 mol/l concentration as in the lower pressure experiments ($p_{ini} = 30$ bar), the first bubble is observed at pressures that are significantly below the 0.2 mol/l contour. This is the case for all three investigated temperatures. However, for all experiments the bubble point pressure increases with temperature. This is in good agreement with the prediction of the van't Hoff equation that CO_2 solubility decreases as temperature increases.

The low-pressure experiments ($p_{ini} = 30$ bar) showed reasonable agreement with van't Hoff theory in terms of predicting when the first free gas bubble was formed. The same cannot be said for the experiments with $p_{ini} = 100$ bar (cf. Fig. 4), where consistent lower bubble point pressures were found than predicted by the van't Hoff equation. Here, we look at the depressurization process for these experiments ($p_{ini} = 100$ bar, $T = 40$, 60, and 100 °C) in greater detail. No bubbles are formed during the heating process even when heating to 100 °C; thus, no nucleation points were present at the start of the depressurization process for any of these experiments. For the 100 °C experiment, this explains that there is no immediate degassing taking place as was the case for the experiment at lower pressure ($p_{ini} = 30$ bar, $T = 100$ °C). However, there are distinct differences in the bubble point pressure, which indicates that some additional physics are involved here. Some possible explanations for this are discussed in Sec. III B.

One of the major changes between experiments is that CO_2 is in its supercritical state for these higher pressure experiments ($p_{crit,CO2} = 73.8$ bar, $T_{crit,CO2} = 31.0$ °C). Thus, a phase change occurs during the depressurization process from supercritical to a gaseous state for the CO_2, which significantly affects the bubble nucleation process. Interestingly, there is no optical change to any of the images at the pressure where the phase change takes place: the images remained free of bubbles until much lower pressures. This shows that even though the optical properties of water with dissolved supercritical CO_2 vs dissolved gaseous CO_2 are the same, the physics of how degassing takes place is nonetheless affected.

During most of the experiments performed here, there is a delay (i.e., a required reduction of pressure) of 2 to 3 bar between the nucleation of the first free gas bubble and the rapid linear increase in the number of bubbles. This delay is of relevance to the application in geothermal reservoirs where large amounts of free gas bubbles can contribute to blocking reservoir pore space as is assumed to have happened at the Groß Schönebeck reservoir in Germany.[25]

B. Influence of other parameters on the degassing process

There are a number of other parameters that may influence the bubble formation process. Some of these, such as the analysis of locations where bubbles form and the evolution of bubble size, are investigated through further examination of the previously obtained data. Some additional experiments have been performed to examine the influence of other parameters, such as the influence of the depressurization rate and the cell's materials. All of these parameters are discussed in this section.

1. Cumulative bubble intensity

To check whether bubbles are formed randomly or are predominantly formed in distinct locations, such as in small scratches on the
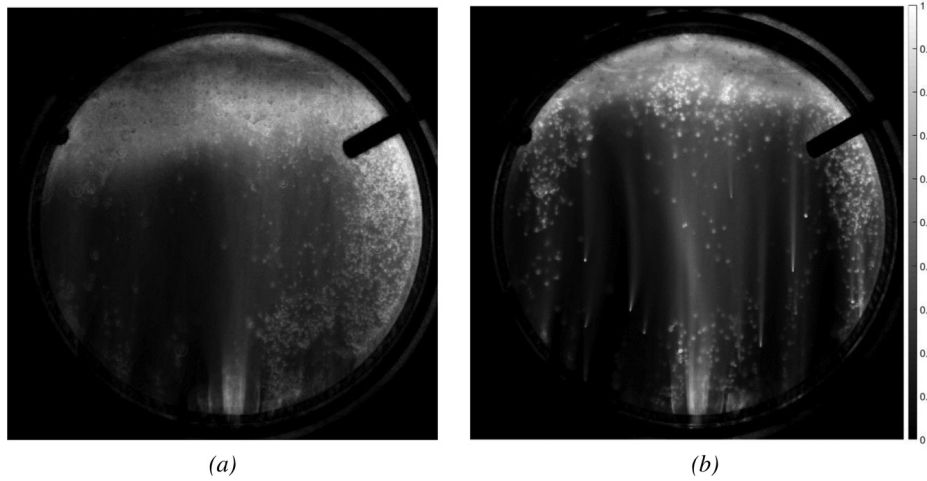
FIG. 5. Normalized cumulative intensity maps of the experiments using 0.2 mol/l CO_2 using the indicated initial pressure and temperature. (a) $p_{ini} = 100$ bar, $T = 100\,°C$, (b) $p_{ini} = 30$ bar, $T = 40\,°C$.

housing or windows of the cell, we have checked cumulative intensity maps of different image series. These are normalized summations of the black and white conversions of the images. Locations where bubbles are present most of the time show up as regions of high intensity on these maps, thus allowing the identification of regions of intense degassing. Figures 5(a) and 5(b) show the resulting intensity maps for the experiments using (a) $p_{ini} = 100$ bar, $T = 100\,°C$ and (b) $p_{ini} = 30$ bar, $T = 40\,°C$. These two different conditions were chosen to see whether pressure and temperature affect the locations of bubble nucleation.

The only two high-intensity regions that show up in both intensity maps are the top and bottom of the visual cell. Both these sites contain sharp edges, which could and do act as a nucleation site for bubbles. Comparing the glass sides of the cell, there are no bubble nucleation regions, which coincide in both experiments. However, in the map for lower initial pressure (30 bar/40 °C), distinct high-intensity bubble trails are present. During a single experiment, preferential regions of bubble nucleation can form, but those same regions do not necessarily carry over between experiments. Within one experiment, at some point the bubble size is such that the buoyancy force is greater than the wall friction, at which point the bubble detaches from the glass and rises in the cell. Some CO_2 from the bubble is left at the surface, and this acts as a nucleation point for the next bubble to form, and thus, the cycle repeats.

2. Influence of initial fluid on bubble formation

The presence and the number of initial nucleation points inside the visual cell were found to be one of the main parameters that control the bubble formation. The 30 bar/100 °C experiment started degassing right from the start, because free gas bubbles were already present within the cell at the pressure and temperature the experiment started. These gas bubbles acted as nucleation points, where bubbles form and grow in size. This implies that using initial conditions where nucleation points such as free gas are present can significantly affect the degassing behavior. To test this idea, a series of experiments were performed at ambient temperature using a 30-bar initial pressure where the initial fluid used to pressurize the cell was varied. The

different initial fluids used here for cell pressurization are nitrogen (N_2) and water (H_2O). The premise is that when using gas as the initial fluid, these molecules adsorb onto imperfections on the cell's surface (windows and steel housing) and serve as points on which new, free gas bubbles can easily start to nucleate. Conversely of the spectrum, water is injected into the cell under vacuum to establish the least nucleation points. The graphs labeled "H_2O" use water pumped into a vacuum in the cell, whereas graphs labeled "H_2O+" use water pumped into a cell containing air. In the latter case, residual air contributes to the number of bubble nucleation sites on the cell's surface, which affects its degassing process, and provides therefore an intermediate number of nucleation points (i.e., more nucleation points than for the H_2O experiments, but not as many as the "N_2" experiments). An overview of the results in terms of bubble point pressure and the maximum number of observed bubbles is given in Fig. 6, where the initial fluid is indicated at the bottom of each bar in the graph. The number of bubbles is indicated here by the gray scale of the bar graphs with darker shades implying more observed bubbles. The quantity plotted here is the logarithm of the maximum number of bubbles [$\log(N_{b,max})$] observed within the single image during the degassing process.
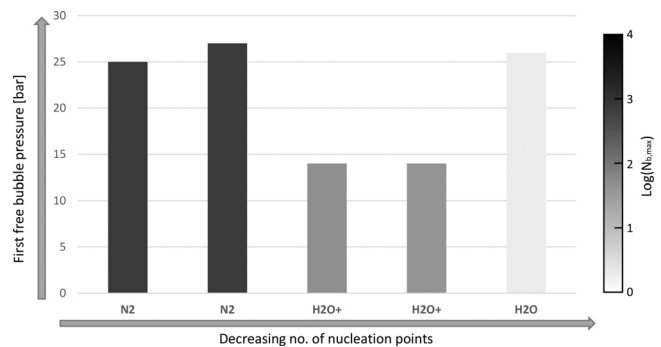

FIG. 6. Pressure where the first free bubble occurs for CO_2 saturated water starting at 30 bar. Initial fluid used to pressurize the cell is given below each bar. Grayscale indicates the peak of the number of bubbles that is formed during the experiment.

This set of experiments is done using water that is fully saturated with CO_2, that is, a concentration of 1.01 mol/l (Henry's law). The concentration here is thus roughly five times higher than in the experiments discussed above. Water and CO_2 are mixed in the transfer vessel at the desired 30-bar pressure with sufficient CO_2 being fed into the vessel to fully saturate the water. The initial fluid on the bubble point pressure correlates well with the number of nucleation points. When using N_2 as the initial fluid, a bubble point pressure is found, which is significantly higher than the 14 bar in the experiments using water and ambient air as the initial fluid (H_2O+). An exception however is observed for water into a vacuum (i.e., the H_2O labeled bar in the figure), for which the bubble pressure is similar to the experiments that start with a nitrogen pressurized cell (26 bar). However, in this H_2O experiment, there was only a single bubble observed at this elevated pressure, and throughout the process, the number of bubbles remained rather low. Using gas as an initial fluid result in up to three orders of magnitudes more bubbles compared to the experiment where water is used as an initial fluid. Results from these experiments are reproducible, with max 2-bar difference in the observed bubble point pressure and similar number of bubbles found. The stark contrast between the number of bubbles observed in the various experiments suggests also a mitigation option for subsurface operations that are hindered by degassing. Rendering a surface fully water-wet is shown here to have the potential to significantly reduce the effects of degassing in processes were free gas bubbles cause problems.

3. Experiments using other pressure cell

The material and surface conditions of the visual cell (i.e., the presence of scratches on the glass or metal parts of the cell) are expected to impact the degassing process. A series of experiments was therefore carried out using another visual of similar dimensions as that used in the experiments discussed above, but made from different material. This cell's housing is made out of titanium, and its windows are sapphire glass as opposed to the stainless steel and borosilicate glass used in the previous experiments. The experiments using the new cell were conducted with the 0.2 mol/l CO_2 concentration that was also used in the previous experiments. Temperatures of 40, 60, and 100 °C were investigated and initial pressures of 30 and 100 bar. Figure 7 shows a comparison in bubble point between the different cells under these conditions. For most experiments, only small differences are observed (~1 bar). The main exception is the 40 °C

experiment using the old cell, which has a significantly lower bubble point compared to the new experiment. The trend that a lower bubble point is observed using a higher initial pressure is found in both sets of experiments though and is thus not considered to be caused by the cell's materials.

4. Lower rate depressurization experiments

A series of experiments was performed at a lower rate of depressurization to assess whether time-dependent kinetics such as the role of diffusion play a significant role in the bubble formation. In these experiments, the depressurization process takes approximately three times longer than in the previous series, while all other conditions were kept the same. The hypothesis here is that bubble formation is diffusion controlled. That is, CO_2 molecules need to diffuse from the solution to the bubble's surface, which can take time. Here, we try to establish whether this time is of significance in the observed bubble points.

These experiments were performed using the titanium cell with sapphire windows and are thus compared with the previous set of experiments using the same cell. To maintain the same frame rate and resolution compared to the other experiments, another camera was used here (Photron FASTCAM NOVA S6) that allows for extended recording time. A total of over 55 000 images were captured for each experiment in this series. The focus here is on experiments with $p_{ini} = 100$ bar, because that is where the largest deviations were observed compared to solubility theory. Figure 8 shows the measured bubble points for both the high and low rates for depressurization. Some differences are present, the largest being the 3-bar difference found for the 100 °C experiment. However, there does not appear to be a clear trend in these differences; that is, the lower rate experiment does not consistently lead to lower or higher bubbles point pressures. Therefore, it assumed that the observed differences are down to measurement errors rather than that they represent a real trend.

5. Influence on equation of state on model prediction

For moderate temperatures, the bubble point pressure can be reasonably predicted using the van't Hoff equation, whereas at higher temperatures, a larger deviation is found. A possible explanation for this is that the value of the term $\frac{-\Delta_{sol}H}{R}$ in this equation is incorrect. A value of 2400 K is used for creating the plots depicted here, but
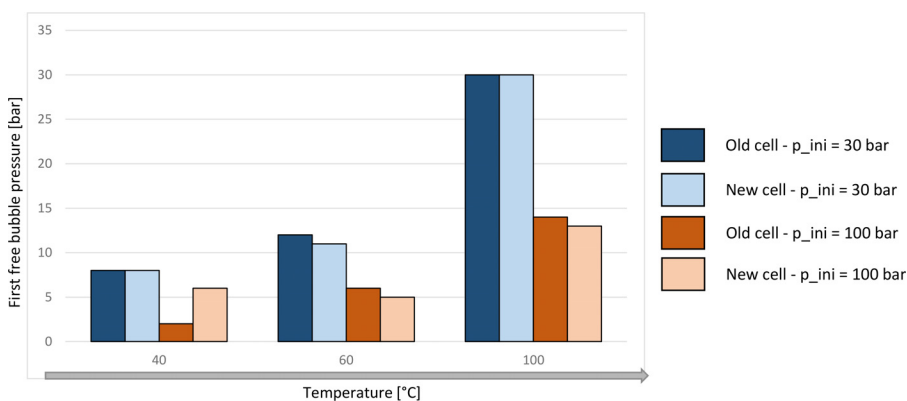

FIG. 7. Comparison of the bubble point between the old and new cell for the indicated conditions.
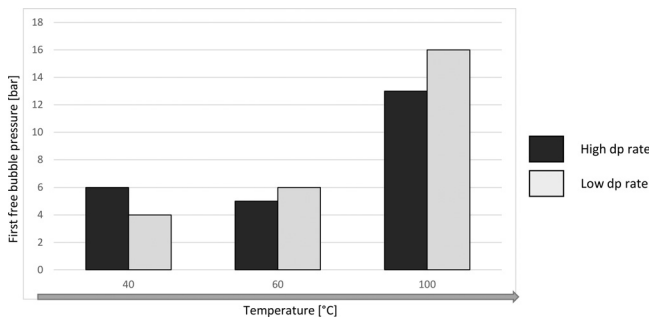
FIG. 8. Comparison bubble points for high and low rates of depressurization ("dp rate").

different values can be found in the literature ranging from 2200 to 2900 K,[48] which would alter the predicted solubility significantly. Other models using a different equation of state are also available. For comparison, here we consider the equation of state from Duan and Sun[38] and see how that affects the predicted solubility. Figure 9 shows the iso-solubility contours for CO_2 in water as a function of the pressure and temperature based on the equation of state of Duan and Sun as opposed to the contours based on the van't Hoff equation in Fig. 4. Experimental results showing the first observed free gas bubble for all the investigated cases are shown as symbols that vary depending on the initial pressure that was used in the experiment [$p_{ini} = 30$ bar (circles), 50 bar (squares) and 100 bar (downward triangles)].

The contours obtained using the equation of state from Duan and Sun are significantly different from those using the van't Hoff equation. The deviation between model prediction and the experiments in the high-temperature regime is somewhat better using this
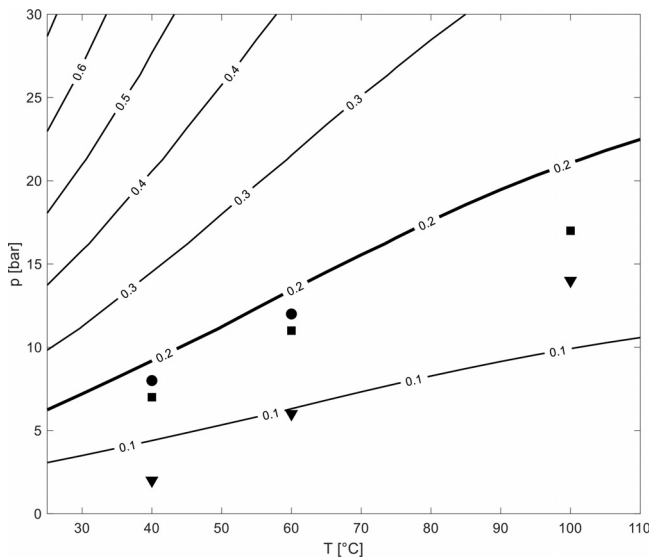

FIG. 9. Iso-solubility contours of CO_2 in water (mol/l) based on a model using the equation of state from Duan and Sun.[38] The 0.2 mol/l contour is given in bold as this is the concentration of CO_2 used in these experiments. Symbols correspond to the observed first free gas bubble during the depressurization experiments for $p_{ini} = 30$ bar (circles), 50 bar (squares), and 100 bar (downward triangles).

equation of state. However, this improved model still does not predict the observed difference between experiments employing different initial pressure and thus different initial CO_2 phase.

6. Analysis of differences in bubble kinetics

A possible explanation for the variation in observed bubble point pressure between experiments with different initial pressure is that the kinetics of bubble formation differ. Different mechanisms during the bubble formation process are investigated here, and assessments are made on their significance in explaining the observed variations. Two mechanisms contribute to bubble growth during the depressurization process: (a) bubble size increases due to gas expansion at lower pressure and (b) CO_2 mass transfer from the surrounding medium into the bubble. Mechanism (a) is studied here by analyzing the average bubble size throughout the degassing process. This is done by computing the equivalent diameter for each bubble as outlined in Sec. II of this manuscript. For bubbles with a short residence time in the cell, mechanism (b) is likely to be dominant due to the limited change in pressure. This mechanism is studied by analyzing the growth of individual bubbles as they ascend within the visual cell.

7. Evolution of average bubble size

Experiments with different initial pressures, but otherwise identical conditions were compared in terms of the average equivalent bubble diameter. This is calculated by summing the equivalent diameters for the individual bubbles and dividing by the number of bubbles within the image. Figure 10 shows the bubble growth during the two experiments at 100 °C ($p_{ini} = 30$ and 100 bar). Symbols (cross or square) represent the average equivalent diameter within a single image. To maintain a readable graph with a limited number of symbols, not every captured image is shown here, but rather the obtained value for every 30th image along with a linear fit to the data for moderate pressures (i.e., below 15 bar) to emphasize the bubble growth behavior in this regime.
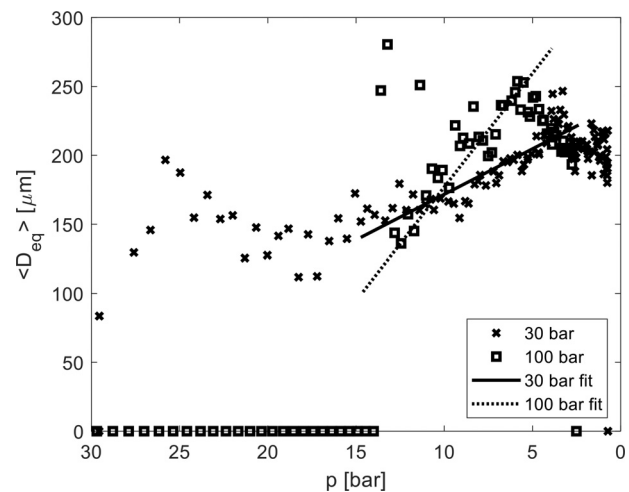

FIG. 10. Comparison of average equivalent bubble diameter $\langle D_{eq} \rangle$ for the experiments at 100 °C and $p_{ini} = 30$ and 100 bar.

At 30 bar, bubbles start forming right from the start, owing to the formation of bubbles during the heating stage. The average bubble size stays fairly constant for the first portion of the depressurization process. However, below ~15 bar, the average bubble size inside the cell increases linearly as the pressure decreases due to gas expansion. For the 100-bar experiment, bubbles are not present at the start, but only start forming only at 14 bar. Below this pressure, a linear increase in bubble size is observed. In this pressure range, the rate of the bubble growth is higher for the 100 bar experiments as there is still more gas in solution compared to the 30-bar experiment at the same pressure where gas was lost during the heating stage. At low pressures (<5 bar), similar average bubble sizes are observed for both experiments.

8. Manual tracking of individual bubbles on images

In addition to variation in bubble size during the degassing process, another question concerns how individual bubbles grow as they ascend within the visual cell. To answer this question, we compare experiments having different initial pressures, at the same stage of depressurization, that is, when pressure reaches the same value, 10 bar. Several bubbles are tracked by eye as they ascend within the cell in consecutive images. On this scale, bubble growth is not dominated by gas expansion due to pressure reduction as the pressure barely decreases within the few analyzed images. Instead, the bubbles' surface acts as a nucleation site for itself causing dissolved CO_2 in the liquid to diffuse to the bubble, which makes it grow.[49] Typically, bubbles in a supersaturated solution grow at a constant rate as they ascend through the liquid independent of their size.[50] Figure 11 shows an example series of black and white conversions of the images around 10 bar for the experiment at 100 °C with p_{ini} = 100 bar. There is a 10-ms interval between the consecutive images shown here to show a distinct rise of the bubbles between each image. The spots on the black background represent individual-free gas bubbles. A number of bubbles have been given a certain color. This allows for individual bubbles to be tracked across multiple images as they ascend through the cell. For example, the red bubble in each of the images in the figure corresponds to the same bubble at different stages of its rise through the cell. The size of the colored bubbles is then analyzed by determining its area and corresponding equivalent diameter. Bubbles of various sizes are present within each image. Figures 12(a)–12(c) show the bubble size for the five colored bubbles as they ascend through the visual cell with p_{ini} = 30, 50, and 100 bar, respectively. The horizontal and vertical

axes in these plots are the same for both experiments to allow for direct comparison. There is a significant margin of error for each bubble due to the limited resolution of the images. Therefore, the error is equal to the pixel size of the images, which is indicated by error bars in these images. Not all bubbles have the same size at the start of their rise through the cell, a range of different diameters is found for each experiment. However, within a single experiment, the bubbles' growth rate is found to be approximately constant. That is, within each experiment, the slope of each line graph is almost identical for all the bubbles observed here. The constant growth rate, independent of bubble size, is in agreement with previous studies.[50,51] This is the case for both the 50- and the 100-bar experiment and similar bubble diameter growth rates are found for both experiments of approximately 2.0×10^3 μm/s; that is, there is a similar CO_2 mass transfer from the surrounding medium into the bubble at 50 and 100 bar. This cannot be said for the 30-bar experiment, which shows a considerably lower bubbles growth rate of around 5.8×10^2 μm/s. A likely cause for this is that for the 30-bar experiment, there were already bubbles forming during the heating stage of the experiment, which results in a lower CO_2 concentration in the liquid during the depressurization. As such, fewer CO_2 molecules can adsorb onto the bubbles' surface, limiting CO_2 mass transfer from bulk solution into the bubble.

C. A mental model of bubble formation during depressurization of CO_2–water mixtures

This section describes the process of CO_2 bubble formation during the depressurization process in a conceptual way. The various aspects and stages of the process are discussed along with parameters of influence. A schematic overview of the process is also presented in Fig. 13.

For most of the experiments discussed here, the depressurization process starts with the CO_2–water mixture as a single homogenous phase. The CO_2 remains in solution until a certain threshold pressure is reached where the solution reaches supersaturation; thus, free gas bubbles start to form [cf. Fig. 13(a)]. This "bubble-point pressure" is dependent of temperature and of CO_2 concentration. Bubbles will first appear on the surfaces of the cell, because CO_2 molecules can accumulate in small scratches and rough patches on the surface.[49] After the initial bubble surface has formed, this surface then allows for more CO_2 molecules to adsorb onto the bubble, causing the bubble to grow. The bubble keeps growing on the surface until the buoyancy force of
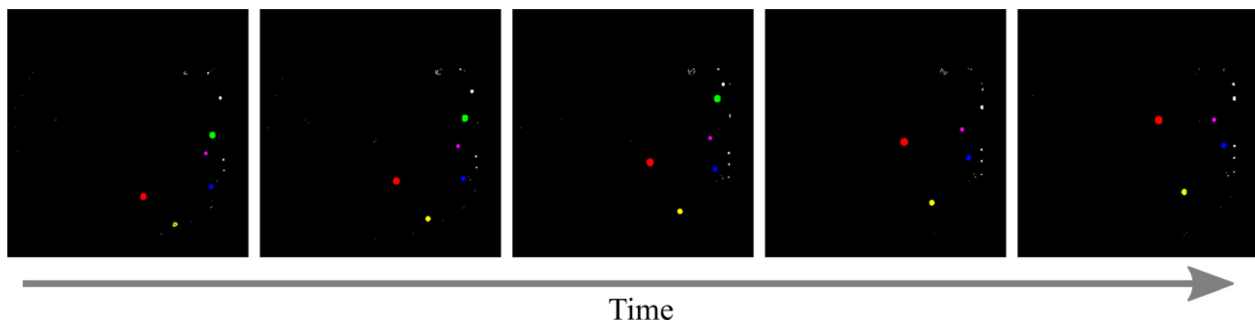

FIG. 11. A series of images at 10 bar showing bubbles at various stages as they ascend in the visual cell. The color of the bubble functions as a label allows an individual bubble to be tracked across multiple images.
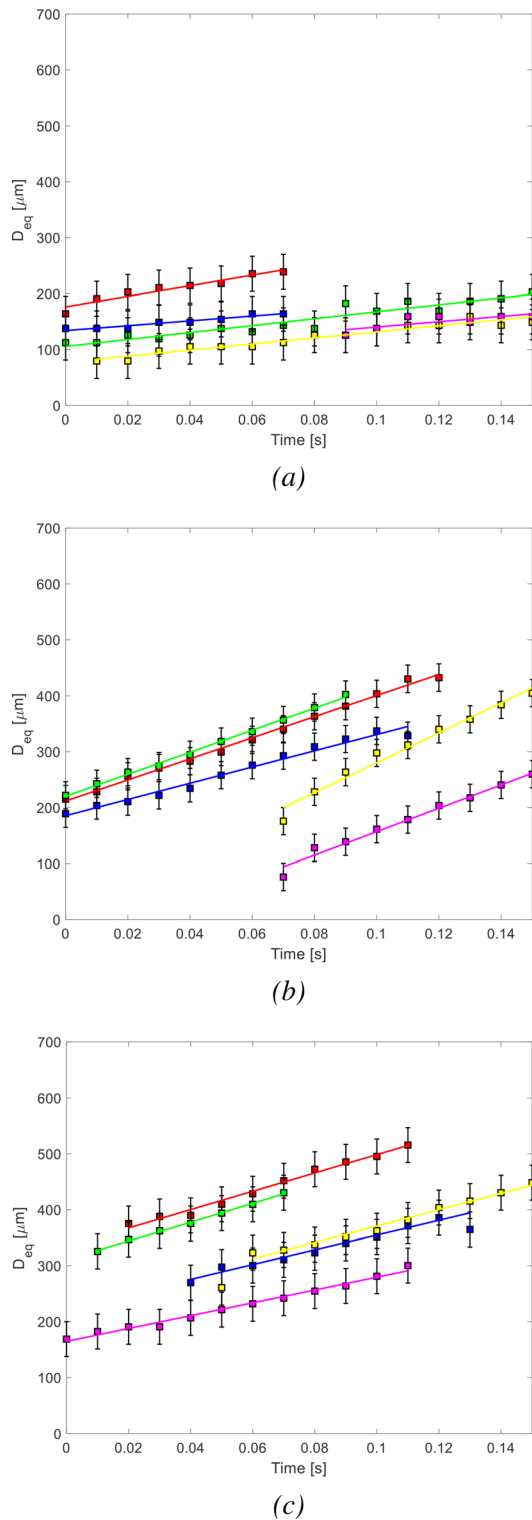
FIG. 12. Bubble size vs time, for five individual bubbles as they ascend in the visual cell at a pressure of 10 bar and 100 °C for (a) $p_{ini} = 30$ bar, (b) $p_{ini} = 50$ bar, and (c) $p_{ini} = 100$ bar.

the bubble is large enough for the bubble to detach from the surface and rise through the liquid [Fig. 13(b)].

Some CO_2 molecules are left on the wall in the location from which the bubble detached, and this will be the site for a new bubble to form. The presence of nucleation sites is a key factor to determine final bubble density. The rising bubbles that have detached from the cell's surface will grow at a constant rate that is independent of their initial size [Fig. 13(c)]. However, the rate at which they grow is dependent on the CO_2 concentration that is still in solution, with higher concentrations causing a more rapid increase in bubble size.

At pressures and temperatures where CO_2 is in the gaseous phase, the pressure at which the first bubble forms can be predicted with reasonable accuracy at ambient temperature using either the van't Hoff equation or the equation of state of Duan and Sun. At elevated temperature, more significant deviations are found. A so far unexplained finding of this study is that the pressure where the first bubble forms is a function of the initial pressure (or initial phase). The experiment with $p_{ini} = 100$ bar with CO_2 in its supercritical state showed between 6- and 16-bar lower bubble point pressure compared to the experiment with $p_{ini} = 30$ bar leads thus increased solubility for all of the experiments investigated here. Several possible explanations for this have been examined including repeat experiments using another visual cell and changing the rate of depressurization. Deviations in bubble point pressure up to 3 bar were found, but without a clear trend in the deviations.

Both the average bubble size throughout the depressurization process and the growth rate of individual bubbles in the experiments at 100 °C have been analyzed. Due to the formation of bubbles in the heating stage for the 30-bar experiment, bubbles start forming there throughout the depressurization process with the average bubble size increasing linearly throughout. For the 100-bar experiment, bubbles only form below 14 bar, but the average bubble size increases more rapidly below this pressure resulting in similar average bubble sizes at low pressure for both experiments. The bubble growth rates for individual bubbles were the same for the 50- and the 100-bar experiments. A much lower growth rate was found for the 30-bar experiment, but this can be attributed to the formation of bubbles during the heating stage of the experiment causing a lower concentration of CO_2 in the solution.

IV. CONCLUSIONS AND RECOMMENDATIONS

- When CO_2 is in a gaseous state, the formation of the first free gas bubbles is in reasonable agreement with the van't Hoff equation, which dictates the solubility of gases at elevated temperatures.
- This is not the case for experiments at higher initial pressure (100 bar) that start out with CO_2 in a supercritical state. Here, the bubble point pressure is consistently lower than the expected bubble point based on the van't Hoff equation.
- Higher temperatures lead to increased deviation from the van't Hoff theory. Better estimates can be established using other equations of state (e.g., Duan and Sun[28]), but deviations still persist.
- At ambient temperature, the degassing process is heavily affected by the presence of nucleation sites, in terms of first bubble formed, and total bubble density, as observed for experiments with different initial fluids. For experiments with $p_{ini} = 30$ bar, up to 12-bar difference is found in bubble point pressure and up
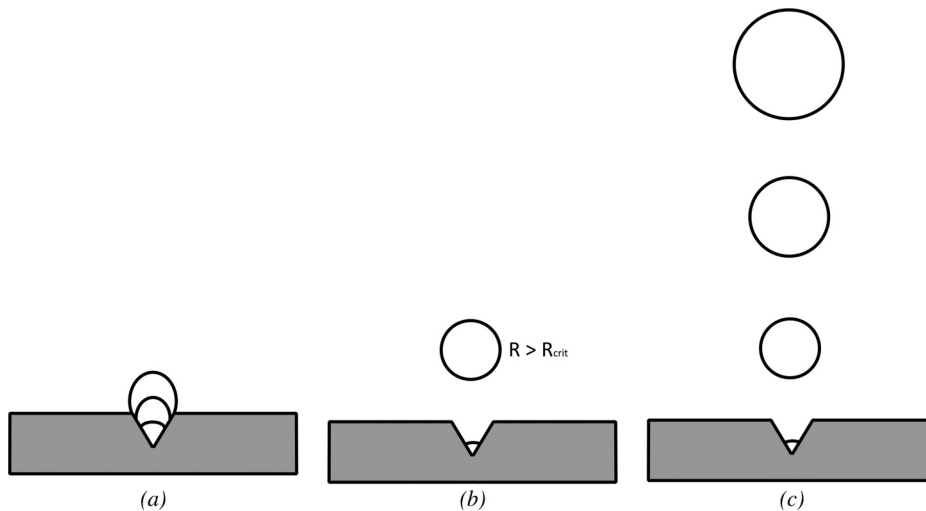
FIG. 13. Schematic overview of the bubble growth process. (a) A bubble forms on a crack in the surface and starts to grow (various stages of the bubble's growth are depicted). (b) Once the bubble has grown larger than the critical radius, it detaches and rises in the liquid leaving behind a small surface in the crack on which the next bubble starts growing. (c) As the bubbles rise through the liquid, dissolved CO_2 molecules will adsorb onto its surface, thus leading to further bubble growth.

to three orders of magnitude in terms of the observed number of bubbles when comparing experiments with high and low number of initial nucleation sites.

- Several possible explanations have been investigated that could cause the dependency of the bubble point pressure, such as the bubble growth rate and the speed of depressurization. The sensitivity analysis to the physical parameters provided no clear indication that it could have a significant impact on the bubble point. This study only provides estimates of the extent to which each of the parameters affects the bubble point pressure. Additionally, more quantitative analysis is recommended to fully understand the physics involved here. Results found in this study can serve as a starting point when setting operating conditions for geothermal water production. Naturally, additional properties of the specific field (e.g., brine salinity) need to be taken into account to limit or prevent the occurrence of degassing.

AUTHOR DECLARATIONS

Conflict of Interest

The authors have no conflicts to disclose.

Author Contributions

Chris Boeije: Conceptualization (supporting); Formal analysis (lead); Investigation (lead); Methodology (lead); Visualization (lead); Writing – original draft (lead). **Pacelli L. J. Zitha:** Funding acquisition (supporting); Project administration (supporting); Supervision (supporting); Writing – original draft (supporting). **Anne Pluymakers:** Conceptualization (lead); Funding acquisition (lead); Investigation (supporting); Methodology (equal); Project administration (lead); Supervision (lead); Writing – original draft (supporting).

DATA AVAILABILITY

The data that support the findings of this study are available upon request from the corresponding author.

REFERENCES

[1] J. Barták, "A study of the rapid depressurization of hot water and the dynamics of vapour bubble generation in superheated water," Int. J. Multiphase Flow **16**, 789 (1990).

[2] E. Y. Kumzerova and A. A. Schmidt, "A numerical simulation of nucleation and dynamics of bubbles formed under drastic depressurization of a liquid," Tech. Phys. **47**, 829 (2002).

[3] G. Liger-Belair, F. Sternenberg, S. Brunner, B. Robillard, and C. Cilindre, "Bubble dynamics in various commercial sparkling bottled waters," J. Food Eng. **163**, 60 (2015).

[4] J. M. Karlsson, M. Gazin, S. Laakso, T. Haraldsson, S. Malhotra-Kumar, M. Mäki, H. Goossens, and W. van der Wijngaart, "Active liquid degassing in microfluidic systems," Lab Chip **13**, 4366 (2013).

[5] H. Cho, J. Kim, and K.-H. Han, "An assembly disposable degassing microfluidic device using a gas-permeable hydrophobic membrane and a reusable microsupport array," Sens. Actuators, B **286**, 353 (2019).

[6] D. D. Meng, J. Kim, and C.-J. Kim, "A degassing plate with hydrophobic bubble capture and distributed venting for microfluidic devices," J. Micromech. Microeng. **16**, 419 (2006).

[7] S. Park, H. Cho, J. Kim, and K.-H. Han, "Lateral degassing method for disposable film-chip microfluidic devices," Membranes **11**, 316 (2021).

[8] H. Puga, J. Barbosa, J. Gabriel, E. Seabra, S. Ribeiro, and M. Prokic, "Evaluation of ultrasonic aluminium degassing by piezoelectric sensor," J. Mater. Process. Technol. **211**, 1026 (2011).

[9] G. Gyarmati, G. Fegyverneki, M. Tokár, and T. Mende, "The effects of rotary degassing treatments on the melt quality of an Al–Si casting alloy," Int. J. Metalcast. **15**, 141 (2021).

[10] D. G. Eskin, "Ultrasonic Degassing of Liquids" in *Power Ultrasonics* (Woodhead Publishing, Oxford, 2015), Chap. 20.

[11]D. Eskin, N. Alba-Baena, T. Pabel, and M. da Silva, "Ultrasonic degassing of aluminium alloys: Basic studies and practical implementation," Mater. Sci. Technol. **31**, 79 (2015).

[12]V. Shaayegan, G. Wang, and C. B. Park, "Study of the bubble nucleation and growth mechanisms in high-pressure foam injection molding through *in-situ* visualization," Eur. Polym. J. **76**, 2 (2016).

[13]X. Xu, D. E. Cristancho, S. Costeux, and Z.-G. Wang, "Bubble nucleation in polymer–CO_2 mixtures," Soft Matter **9**, 9675 (2013).

[14]C. Wang, *Bubble Dynamics in High-Pressure Foam Injection Molding* (University of Toronto, Toronto, 2022).

[15]Y. Fu, W. van Berk, and H.-M. Schulz, "Temporal and spatial development of scale formation: One-dimensional hydrogeochemical transport modeling," J. Pet. Sci. Eng. **112**, 273 (2013).

[16]R. d P. Cosmo, F. d A. Ressel Pereira, D. D. C. Ribeiro, W. Q. Barros, and A. L. Martins, "Estimating CO_2 degassing effect on $CaCO_3$ precipitation under oil well conditions," J. Pet. Sci. Eng. **181**, 106207 (2019).

[17]G. Garven, "Fault-related CO_2 degassing, geothermics, and fluid flow in southern California basins: Physiochemical evidence and modeling," Technical Report No. DOE-TUFTS-15900 (Tufts University, 2015).

[18]V. I. Ivannikov, I. V. Ivannikov, and T. W. Bakker, "Production improvement by controlling the flow regime of gas rich fluid mixtures with slugging devices," presented at the Middle East Oil Show (Bahrain, June 2003), pp. SPE-81453-MS.

[19]T. Groth, A. Luke, D. Mewes, and M. Reichwage, "Effects of dissolving and degassing phenomena on multiphase oil and gas boosting," in 14th International Conference on Multiphase Production Technology (2009).

[20]Z. Qin, M. Arshadi, and M. Piri, "Carbonated water injection and *in situ* CO_2 exsolution in oil-wet carbonate: A micro-scale experimental investigation," Energy Fuels **35**, 6615 (2021).

[21]S. Arnórsson, "Deposition of calcium carbonate minerals from geothermal waters: Theoretical considerations," Geothermics **18**, 33 (1989).

[22]A. Stefánsson, N. S. Keller, J. G. Robin, H. Kaasalainen, S. Björnsdóttir, S. Pétursdóttir, H. Jóhannesson, and G. Ó. Hreggvidsson, "Quantifying mixing, boiling, degassing, oxidation and reactivity of thermal waters at Vonarskard, Iceland," J. Volcanol. Geotherm. Res. **309**, 53 (2016).

[23]S. Taweelarp, S. Suntikoon, T. Rojsiraphisal, N. Ploymaklam, and S. Saenton, "Geochemical modeling of scale formation due to cooling and CO_2-degassing in San Kamphaeng Geothermal Field, Northern Thailand," Chiang Mai Univ. J. Nat. Sci. **20**, e2021049 (2021).

[24]G. Pátzay, G. Stáhl, F. H. Kármán, and E. Kálmán, "Modeling of scale formation and corrosion from geothermal water," Electrochim. Acta **43**, 137 (1998).

[25]G. Blöcher, T. Reinsch, J. Henninges, H. Milsch, S. Regenspurg, J. Kummerow, H. Francke, S. Kranz, A. Saadat, G. Zimmermann, and E. Huenges, "Hydraulic history and current state of the deep geothermal reservoir Groß Schönebeck," Geothermics **63**, 27 (2016).

[26]G. Chiodini, A. Baldini, F. Barberi, M. L. Carapezza, C. Cardellini, F. Frondini, D. Granieri, and M. Ranaldi, "Carbon dioxide degassing at Latera caldera (Italy): Evidence of geothermal reservoir and evaluation of its potential energy," J. Geophys. Res. **112**, 004896, https://doi.org/10.1029/2006JB004896 (2007).

[27]F. Frondini, S. Caliro, C. Cardellini, G. Chiodini, and N. Morgantini, "Carbon dioxide degassing and thermal energy release in the Monte Amiata volcanic-geothermal area (Italy)," Appl. Geochem. **24**, 860 (2009).

[28]F. Rodríguez, N. M. Pérez, G. V. Melián, E. Padrón, P. A. Hernández, M. Asensio-Ramos, G. D. Padilla, J. Barrancos, and L. D'Auria, "Exploration of deep-seated geothermal reservoirs in the Canary Islands by means of soil CO_2 degassing surveys," Renewable Energy **164**, 1017 (2021).

[29]L. Peiffer, G. Carrasco-Núñez, A. Mazot, R. E. Villanueva-Estrada, C. Inguaggiato, R. B. Romero, R. Rocha Miller, and J. H. Rojas, "Soil degassing at the Los Humeros geothermal field (Mexico)," J. Volcanol. Geotherm. Res. **356**, 163 (2018).

[30]A. Sbrana, P. Marianelli, M. Belgiorno, M. Sbrana, and V. Ciani, "Natural CO_2 degassing in the Mount Amiata volcanic–geothermal area," J. Volcanol. Geotherm. Res. **397**, 106852 (2020).

[31]L. Shen, K. Wu, Q. Xiao, and D. Yuan, "Carbon dioxide degassing flux from two geothermal fields in Tibet, China," Chin. Sci. Bull. **56**, 3783 (2011).

[32]T. L. V. Bornemann, P. S. Adam, V. Turzynski, U. Schreiber, P. A. Figueroa-Gonzalez, J. Rahlff, D. Köster, T. C. Schmidt, R. Schunk, B. Krauthausen, and A. J. Probst, "Geological degassing enhances microbial metabolism in the continental subsurface," bioRxiv (2020).

[33]A. Aiuppa, C. Federico, G. Giudice, S. Gurrieri, M. Liuzzo, H. Shinohara, R. Favara, and M. Valenza, "Rates of carbon dioxide plume degassing from Mount Etna volcano," J. Geophys. Res. **111**, 04307, https://doi.org/10.1029/2006JB004307 (2006).

[34]A. Caracausi, F. Italiano, A. Paonita, A. Rizzo, and P. M. Nuccio, "Evidence of deep magma degassing and ascent by geochemistry of peripheral gas emissions at Mount Etna (Italy): Assessment of the magmatic reservoir pressure," J. Geophys. Res. **108**, 02095, https://doi.org/10.1029/2002JB002095 (2003).

[35]P. J. Carvalho, L. M. C. Pereira, N. P. F. Gonçalves, A. J. Queimada, and J. A. P. Coutinho, "Carbon dioxide solubility in aqueous solutions of NaCl: Measurements and modeling with electrolyte equations of state," Fluid Phase Equilib. **388**, 100 (2015).

[36]H. Zhao, M. V. Fedkin, R. M. Dilmore, and S. N. Lvov, "Carbon dioxide solubility in aqueous solutions of sodium chloride at geological conditions: Experimental results at 323.15, 373.15, and 423.15 K and 150 bar and modeling up to 573.15 K and 2000 bar," Geochim. Cosmochim. Acta **149**, 165 (2015).

[37]J. L. Cruz, E. Neyrolles, F. Contamine, and P. Cézac, "Experimental study of carbon dioxide solubility in sodium chloride and calcium chloride brines at 333.15 and 453.15 K for pressures up to 40 MPa," J. Chem. Eng. Data **66**, 249 (2021).

[38]Z. Duan and R. Sun, "An improved model calculating CO_2 solubility in pure water and aqueous NaCl solutions from 273 to 533 K and from 0 to 2000 bar," Chem. Geol. **193**, 257 (2003).

[39]J. Li, L. Wei, and X. Li, "Modeling of CO_2-CH_4-H_2S-brine based on cubic EOS and fugacity-activity approach and their comparisons," Energy Procedia **63**, 3598 (2014).

[40]P. F. dos Santos, L. André, M. Ducousso, A. Lassin, F. Contamine, A. Lach, M. Parmentier, and P. Cézac, "An improved model for CO_2 solubility in aqueous Na^+-Cl^--SO_4^{2-} systems up to 473.15 K and 40 MPa," Chem. Geol. **582**, 120443 (2021).

[41]C. F. Delale, J. Hruby, and F. Marsik, "Homogeneous bubble nucleation in liquids: The classical theory revisited," J. Chem. Phys. **118**, 792 (2003).

[42]S. L. Meadley and F. A. Escobedo, "Thermodynamics and kinetics of bubble nucleation: Simulation methodology," J. Chem. Phys. **137**, 074109 (2012).

[43]G. Liger-Belair, "Carbon dioxide in bottled carbonated waters and subsequent bubble nucleation under standard tasting condition," J. Agric. Food Chem. **67**, 4560 (2019).

[44]S. Uzel, M. A. Chappell, and S. J. Payne, "Modeling the cycles of growth and detachment of bubbles in carbonated beverages," J. Phys. Chem. B **110**, 7579 (2006).

[45]R. W. Henley, A. H. Truesdell, P. B. Barton, Jr., and J. A. Whitney, *Fluid-Mineral Equilibria in Hydrothermal Systems* (Society of Economic Geologists, 1984).

[46]J. Haizlip, M. Stover, S. Garg, F. Tut Haklidir, and N. Prina, *Origin and Impacts of High Concentrations of Carbon Dioxide in Geothermal Fluids of Western Turkey* (Stanford University, Stanford, CA, 2016).

[47]F. L. Smith and A. H. Harvey, "Avoid Common Pitfalls when using Henry's Law" Chem. Eng. Progress **103**(9), 33–39 (2007).

[48]R. Sander, "Compilation of Henry's law constants (version 4.0) for water as solvent," Atmos. Chem. Phys. **15**, 4399 (2015).

[49]N. E. Shafer and R. N. Zare, "Through a beer glass darkly," Phys. Today **44**(10), 48 (1991).

[50]R. Zenit and J. Rodríguez-Rodríguez, "The fluid mechanics of bubbly drinks," Phys. Today **71**(11), 44 (2018).

[51]G. Liger-Belair, "The physics and chemistry behind the bubbling properties of champagne and sparkling wines: A state-of-the-art review," J. Agric. Food Chem. **53**, 2788 (2005).